A Preliminary Engineering Design of Intravascular Dual-Frequency Transducers for Contrast-Enhanced Acoustic Angiography and Molecular Imaging

Jianguo Ma, K. Heath Martin, Paul A. Dayton, and Xiaoning Jiang

Abstract—Current intravascular ultrasound (IVUS) probes are not optimized for contrast detection because of their design for high-frequency fundamental-mode imaging. However, data from transcutaneous contrast imaging suggests the possibility of utilizing contrast ultrasound for molecular imaging or vasa vasorum assessment to further elucidate atherosclerotic plaque deposition. This paper presents the design, fabrication, and characterization of a small-aperture (0.6 × 3 mm) IVUS probe optimized for high-frequency contrast imaging. The design utilizes a dual-frequency (6.5 MHz/30 MHz) transducer arrangement for exciting microbubbles at low frequencies (near their resonance) and detecting their broadband harmonics at high frequencies, minimizing detected tissue backscatter. The prototype probe is able to generate nonlinear microbubble response with more than 1.2 MPa of rarefractional pressure (mechanical index: 0.48) at 6.5 MHz, and is also able to detect microbubble response with a broadband receiving element (center frequency: 30 MHz, −6-dB fractional bandwidth: 58.6%). Nonlinear super-harmonics from microbubbles flowing through a 200-μm-diameter micro-tube were clearly detected with a signal-to-noise ratio higher than 12 dB. Preliminary phantom imaging at the fundamental frequency (30 MHz) and dual-frequency super-harmonic imaging results suggest the promise of small aperture, dual-frequency IVUS transducers for contrast-enhanced IVUS imaging.

I. Introduction

It is well known that atherosclerotic cardiovascular disease is a leading cause of death worldwide, and one which often manifests without warning [1]. For up to 75% of acute coronary syndromes, the underlying pathological mechanism is hypothesized to be atherosclerotic plaque rupture [1]. Unfortunately, a high percentage of vulnerable plaques are also angiographically occult (nonstenotic), and these are responsible for a high proportion of ensuing cardiac events resulting in either fatalities or requiring further interventional treatment [2], [3]. For this reason, detection and characterization of plaques which are rupture prone is one of the most active areas of research in cardi-

ology and biomedical imaging [4]. The vasa vasorum is a network of microvessels which supports larger vessels such as the aorta, and increased density of the vasa vasorum has been associated with a plaque advancing from a stable state to a rupture-prone state [5], [6]. Additionally, intraplaque hemorrhage occurring from thin-walled, immature microvessels has been present in plaques in many cases of sudden coronary death [7]. Evidence suggests that vasa vasorum proliferation and associated angiogenesis and inflammation is associated with plaque instability and rupture [7]–[10]. Because our ability to predict the instability of atherosclerotic lesions remains a substantial challenge, there is an unmet need for new imaging methods to identify, detect, and differentiate these pathologies [11].

The new technology of ultrasound molecular imaging utilizes contrast agents displaying targeting ligands to identify areas of inflammation and angiogenesis associated with disease progression (targets that cannot be identified by B-mode ultrasound) [12]–[14]. Prior data suggests that ultrasound molecular imaging will provide a unique opportunity for plaque biomarker evaluation (such as inflammatory or angiogenic markers) and for identification of vulnerable plaques [15]. Additionally, a new high-frequency contrast imaging technique, acoustic angiography [16], takes advantage of exciting microbubbles near resonance and detecting their high-frequency, broadband harmonics with sufficient bandwidth separation to achieve both high resolution and high contrast-to-noise ratio (CNR). Data has shown that acoustic angiography enables detailed visualization and analysis of microvascular structure [16], [17], and will likely be applicable to vasa vasorum imaging. Thus, we hypothesize that there is a role for contrast-enhanced ultrasound imaging in the assessment of atherosclerosis.

Feinstein has illustrated the potential of contrast enhanced transcutaneous ultrasound imaging on the carotid artery [18], but the potential of transcutaneous ultrasound has limitations with resolution and motion artifacts [19], especially if the target is the deeper coronary arteries. This may present an opportunity for intravascular ultrasound (IVUS), although commercial IVUS systems have lacked contrast-enhanced imaging capability. This absence of technology may be due to the fact that nonlinear detection strategies for contrast imaging are most effective near the resonant frequency of microbubble contrast agents, which is typically between 1 and 10 MHz [20]. Thus, con-

ventional contrast imaging strategies are not very effective with high-frequency ultrasound (35 to 50 MHz) that is typically used with IVUS. To overcome this challenge, Goertz and collaborators have been evaluating both subharmonic and harmonic contrast IVUS imaging, with the goal of vasa vasorum imaging [3], [21]. Their research showed a contrast-to-tissue ratio (CTR) of 28 dB in subharmonic imaging with a fundamental frequency of 30 MHz [3] and 25 dB in second-harmonic imaging with a fundamental frequency of 20 MHz [21].

We hypothesize that resolution and contrast to tissue ratios can be further improved over subharmonic or harmonic contrast IVUS imaging by excitation of microbubbles near resonance and detecting their backscatter at a bandwidth substantially higher than that of the transmission, previously called super-harmonic, ultra-broadband, or transient imaging. In prior work, de Jong *et al.* [22], Bouakaz *et al.* [23], and Kruse and Ferrara [24] demonstrated that substantial improvements in CTR could be achieved by detecting the high-frequency energy produced by microbubbles excited at lower frequencies. Bouakaz *et al.* utilized a dual-frequency transducer to illustrate that the CTR of the fourth and fifth harmonic could be 15 and 7 dB higher than that of the second harmonic, respectively [23]. Kruse *et al.* also utilized a dual-frequency transducer arrangement and demonstrated that substantial scattered energy from microbubbles excited near 2 MHz could be detected at a frequency as high as 45 MHz. More recently, Gessner *et al.* [16], [17], [25] utilized mechanically-scanned dual-frequency transducers (transmit at 2 or 4 MHz; receive at 30 MHz) on the VisualSonics Vevo770 (VisualSonics Inc., Toronto, ON, Canada) to perform high-frequency 3-D contrast imaging of *in vivo* microvasculature and achieved resolution on the order of 100 μm with a CTR high enough that microvessels could be readily segmented from the images and their morphology analyzed.

Despite the promising CTR and vessel imaging capability of this imaging approach, there is a substantial challenge for ultra-broadband contrast-enhanced intravascular ultrasound (CE-IVUS), which is likely why it is still relatively undeveloped. The primary limitation is the large frequency span, which is outside of the current bandwidth of commercially available single-frequency transducers. Such difficulty could be surmounted by using multiple confocal transducers as described by Gessner [25], however dual-frequency transducers of the necessary frequency range do not yet exist in a form factor required for IVUS.

In this paper, we demonstrate the design, fabrication, and characterization of a small aperture, dual-frequency IVUS transducer which provides sufficient bandwidth separation for high CTR, high-resolution CE-IVUS imaging.

II. Materials and Methods

A. Transducer Design and Fabrication

The dual-frequency transducer was designed as a dual layer transduction structure, composed of a low-frequency transmitting layer and a high-frequency receiving layer (Fig. 1) [26]. The transmission layer was placed behind the receiving layer (with respect to a forward-traveling sound wave) because low-frequency transmitted acoustic waves could propagate through the smaller, high-frequency element. The placement of the receiving layer has little interference on the transmission because of its small thickness (65 μm) compared with the transmitting wavelength (616 μm). The selection of 6.5 MHz as the transmitting layer's center frequency was chosen because it was both close to the contrast agents' resonant frequency and because the piezoelectric material for this element was readily available. The high-frequency receiving layer was positioned in the front of the transducer to minimize the interference from the transmitting layer. A frequency-selective isolation layer with a quarter-wavelength of 30 MHz [27] was placed between the two piezoelectric layers to allow the low-frequency transmitting wave to pass through, but the high-frequency receiving wave to be reflected at the isolation interface. Transducer dimensions were optimized using a Krimholtz–Leedom–Matthaei (KLM) model [28] to validate the thickness of layers, length, and width of each component for ideal thickness mode excitation. Material properties and final optimized parameters for modeling and fabrication are summarized in Table I. The aperture of the high-frequency receiving layer was designed to be similar to that of commercial IVUS transducers [29], and thus significantly smaller than that of the transmission layer. The relatively large aperture of the low-frequency component was designed to obtain reasonably low electrical impedance at low frequencies for higher acoustic pressure transmission. The modeling of the 30-MHz element considered the existence of the 6.5-MHz element at Side B (back side) as backing according to the structure of the design in Fig. 1. The design of the transducer used lead magnesium niobate-lead titanate (PMN-PT) instead of polyvinylidene fluoride (PVDF) as the receiving layer for higher sensitivity because [30]: 1) PMN-PT has a much higher piezoelectric and electromechanical coupling coefficient than PVDF, and 2) the dielectric constant of PMN-PT is 400 to 600 times higher than that of PVDF, making it easier to match the electrical impedance to the receiving system.

In the fabrication of the dual-frequency transducer, a 5 × 5 mm piezoelectric acoustic stack was first assembled and then diced into 0.6-mm-wide slices as individual transducers. The assembly process started with a 5 × 5 mm PMN-PT plate which was lapped to 300 μm ($f =$ 6.5 MHz) in thickness and then coated with Ti/Au (Ti: 10 nm and Au: 100 nm; E-Beam, Jefferson Hills, PA) on both surfaces (Fig. 2, step 1). A second piece of PMN-PT (0.5 × 5 × 0.3 mm) was then bonded on the first PMN-PT layer using conductive silver epoxy to form the high-frequency receiving element and frequency-selective isolation layer. Polystyrene microspheres (Polysciences Inc., Warrington, PA) having a nominal diameter of 10 μm were added (about 1% in volume) to the silver epoxy so that the thickness of bonding layer was controlled to be
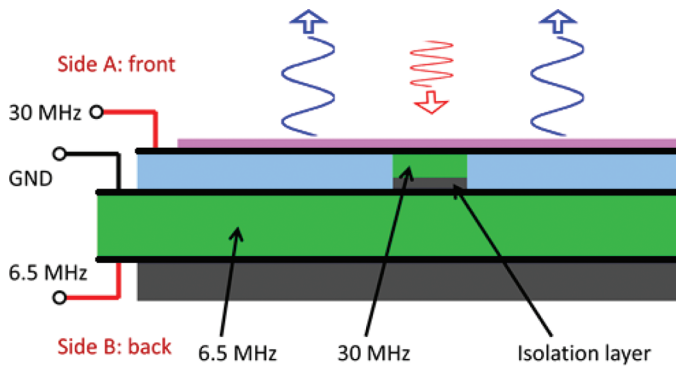
Fig. 1. Design of the dual-frequency IVUS transducer.

Fig. 2. Fabrication process diagram of the dual-frequency transducer.

13 to 15 μm to function as a frequency-selective isolation layer previously mentioned (Fig. 2, step 2). After the silver epoxy cured, a composite layer of Al_2O_3 powder (1 μm grain size, Logitech Ltd., Glasgow, UK) and Epo-tek 301 (Epoxy Technology Inc., Billerica, MA) was mixed 1:1 by weight and centrifuged at 10 000 rpm (5590 g) for 10 min (Microfuge Lite, Beckman Coulter Inc., Brea, CA). The prepared composite was then cast onto the front of the 5 × 5 mm PMN-PT layer beside the 0.5-mm-width slice. A small margin (0.5 mm) at one edge was left as an electrical connection site for later wiring. After the Al_2O_3/epoxy composite cured, it was then lapped until the bonded composite layer was 80 μm thick, making the thickness of the top PMN-PT layer 65 μm ($f = 30$ MHz) on top of the 15-μm isolation layer (Fig. 2, step 3). Another Ti/Au layer (Ti: 10 nm and Au: 100 nm) was then deposited onto the top surface to form the top electrodes. The final stack was then diced into 0.6-mm-wide slices to form individual dual-frequency transducers (Fig. 2, step 4). Each slice was bonded to the tip of a 20-gauge hypodermic needle (Fisher Scientific International Inc., Hampton, NH) and then coated with a layer of parylene film (15 μm). The parylene film served two purposes: 1) to act as a matching layer of the 30-MHz high-frequency element, and 2) to provide electrical isolation in the form of a passivation
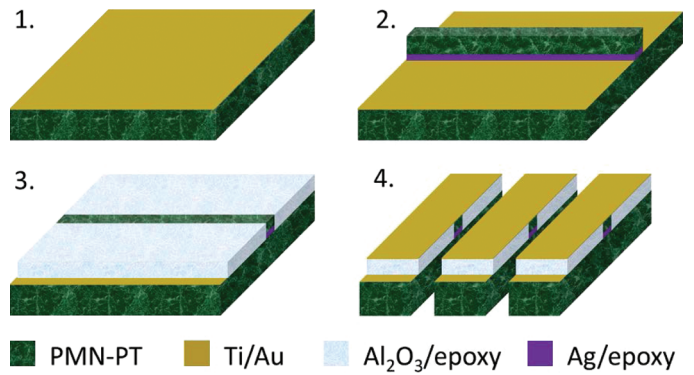
layer for the entire transducer. Finally, the transducer was poled with a dc electrical field of 10 kV/cm for 15 min in silicone oil at room temperature.

After the transducers were poled, electrical characteristics such as capacitance, loss, and input electrical impedance were characterized using an Agilent 4294A precision impedance analyzer (Agilent Technologies Inc., Santa Clara, CA). Capacitance and loss were measured at 1 kHz and the input electrical impedance was measured near the resonant frequency of each element, individually.

B. Acoustic Characterization

The main design consideration for the low-frequency (6.5 MHz) transmission element was to deliver adequate peak negative pressure (e.g., > 1 MPa) to produce detectable nonlinear oscillations of microbubble contrast agents. The peak negative pressure of the small aperture transducer was measured using a calibrated needle hydrophone (HNA-0400, Onda Corp., Sunnyvale, CA) positioned axially at 3 mm away from the transducer. This distance was kept constant between pressure measurements and subsequent microbubble tests to estimate pressure levels applied to the contrast agents. The excitation pulse used

TABLE I. Fabrication Parameters of the Dual-Frequency Transducer.

| Parameter	6.5 MHz layer	30 MHz layer
Active material	PMN-PT	PMN-PT
Thickness (μm)	300	65
Width (mm)	0.6	0.6
Length (mm)	3	0.5
Sound speed (m/s)	4004	4004
Impedance (MRayl)	32	32
Matching material	Al_2O_3/epoxy	Parylene
Thickness (μm)	80	15
Sound speed (m/s)	1600	2770
Impedance (MRayl)	4.32	3.16
Attenuation (dB/cm per MHz)	5.3	0.1
Backing material	Ag/epoxy	Ag/epoxy (isolation)
Thickness (μm)	200	15
Sound speed (m/s)	1900	1900
Impedance (MRayl)	5.15	5.15
Attenuation (dB/cm per MHz)	8	8
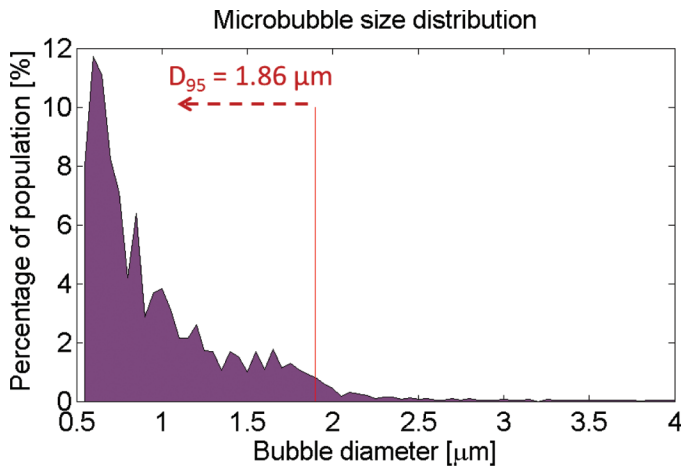
Fig. 3. Microbubble size distribution.

was a sinusoidal burst (1 to 5 cycles) at 6.5 MHz generated by an arbitrary function generator (AFG3101, Tektronix Inc., Beaverton, OR) and amplified by 55 dB with a radio-frequency amplifier (Model 3200L, Electronic Navigation Industries Inc., Rochester, NY). The amplitude of the transmission signal was adjusted from 50 to 350 mV (peak-to-peak) before amplification. Pressure output of the transducer was recorded using an in-house LabVIEW (National Instruments Co., Austin, TX) data acquisition system.

The receive element design optimized both reception sensitivity and bandwidth, which is critical for detection of the broadband, nonlinear microbubble signal. Pulse–echo tests were performed to measure the bandwidth of the transducer. A steel block with a flat surface was positioned 3 mm in front of the transducer as the target. A pulser/receiver (5900PR, Panametrics Inc., Waltham, MA) was used to interrogate the target in pulse–echo mode with minimal energy. The reflected signal was high-pass filtered (f_c = 3 MHz) by the pulser/receiver and then recorded using a digital oscilloscope (DSO7104B, Agilent Technologies Inc., Santa Clara, CA). Loop sensitivity was measured with a similar setup, but the excitation signal was replaced by a 10-cycle sinusoidal burst.

C. Contrast Detection by the Transducer

To validate the contrast response of the transducer, microbubbles were excited by the low-frequency element and the nonlinear responses from microbubbles were detected using the high-frequency element. Relative positions of the transducer and the tube were carefully adjusted in a water bath using a 3-axis precision rectilinear stage. In the alignment process, an acoustically transparent 200-μm-diameter microtube was filled with air to provide a strong echo to indicate alignment in the lateral dimension of the 30-MHz element. Time of arrival of the echo was used to calculate the distance between the transducer and the tube to position it axially 3 mm away from the trans-

ducer. Polydisperse lipid-shelled microbubbles (Fig. 3) were formulated as described previously [31] and pumped through the aligned micro-tube at a concentration of 4.8 × 10^8 microbubbles/mL at a velocity between 1.8 and 4.4 cm/s to maximize the signal response. The tube was slightly angled (∼10°) with respect to the front surface of the transducer to reduce specular reflections from the wall of the tube.

Once the transducer was aligned and positioned for the contrast imaging, the excitation pulse sequence was adjusted for optimal imaging quality. A sinusoidal burst was used to excite the transmitting element with pulse lengths between 1 to 5 cycles and voltage variations from 50 to 350 mV_{pp} in 50 mV_{pp} increments. For each combination of testing parameters, 100 A-lines of microbubble echoes were received and recorded by the high-frequency element for offline analysis. The contrast imaging data was evaluated using both time-domain amplitude analysis and short-time Fourier transform.

D. Imaging With the Transducer

Fundamental imaging at 30 MHz and dual-frequency super-harmonic contrast imaging were tested with the transducer in tissue-mimicking phantoms immersed in water (Fig. 4). Typical phantoms had a speed of sound similar to tissue (1496 m/s), relatively high attenuation (0.9 dB/cm at 3 MHz), and had fully developed speckle. A hole was drilled through the phantom using a thin-walled steel tube (5.5 mm OD, 0.4 mm wall thickness) to simulate a vessel. After drilling, the dual-frequency probe was placed in the center of the lumen and rotated to make an IVUS image. The rotation was controlled using a microcontroller that stepped the transducer at 0.9° angular increments for one revolution and provided a trigger for the excitation pulse. An acoustically transparent tube with 200-μm-diameter was placed through the phantom, running parallel to the channel. Diluted microbubbles were pumped through the tube (4.4 cm/s) while imaging. A 0.6-mm-diameter steel rod was placed in the phantom opposite the microbubble tube to provide a strong reflection target for comparison. Both the microbubble tube and the steel rod were embedded at ∼4 mm radially in the phantom to test whether the system could detect contrast in a scattering and attenuating medium, which is typical of tissue.

For fundamental imaging, both acoustic excitation and signal reception were performed using the 30-MHz element. A pulser/receiver supplied the transducer with a 1 μJ excitation pulse at every step and the reflected signal was recorded by the LabVIEW data acquisition system described previously. For super- harmonic imaging, a 2-cycle sinusoidal burst was amplified by the 3200L RF amplifier to excite the 6.5-MHz transducer while the 30-MHz element was used for receiving. The data was digitally band-pass filtered with a frequency window of 25 to 35 MHz corresponding to the receive element's band-
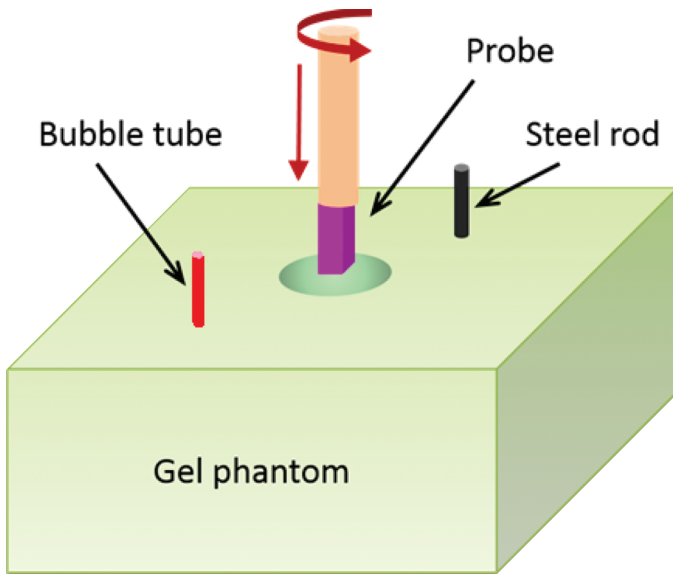
Fig. 4. Experimental setup for the imaging.

Fig. 5. Prototype transducer housed on the tip of a 20-gauge hypodermic needle.

width. The acquired A-lines were then envelope detected and scan converted to an IVUS image where the CTR was measured by using regions of interest to calculate the mean signal strength.

III. Results and Discussion

The dual-frequency transducer prototype was housed on the tip of a 20-gauge hypodermic needle (Fig. 5). The back surface (Side B in Fig. 1) of the transducer was bonded to the needle with conductive epoxy, allowing the needle to function as an electrical lead to the back side of the 6.5-MHz transducer. Co-axial wires (25 gauge) were attached to the top electrode and common electrode between the two PMN-PT layers and then threaded through the needle.

A. Electrical Characterization

The capacitance and loss at 1 kHz (measured with an Agilent 4294A precision impedance analyzer) showed good agreement with predicted values. Capacitance values of the transducers were 344 pF for the 6.5-MHz transmission element and 131 pF (including a 2 pF parasitic capacitance from the Al_2O_3/epoxy layer) for the 30-MHz receiving element. This data was in agreement with theoretical calculations using a relative dielectric constant of 4000 (HC Materials, Inc.). Loss of the transducer was 1.1% for transmission and 2.7% for reception, similar to the properties of PMN-32%PT.

The measured input electrical impedance at the resonant frequency [Figs. 6(b) and 6(d)] matched well with the results of the KLM modeling [Figs. 6(a) and 6(c)]. To obtain a strong resonance for high-pressure output in the transmission element, the backing layer of the transmis-
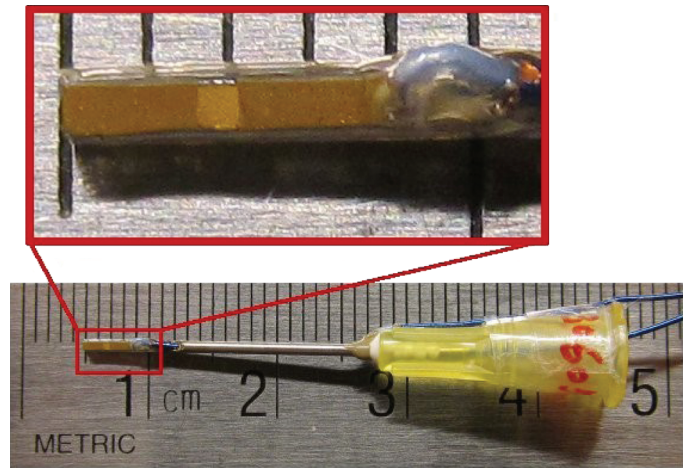
sion element was designed with reasonable absorption for compromise of achieving sufficient pressure output while minimizing ringing. In both the modeling and measured results, a strong resonance occurred at 6.5 MHz [Figs. 6(a) and 6(b)]. The center frequency of the receiving element was designed to be 30 MHz [Figs. 6(c) and 6(d)] and the measured results agreed very well with simulations.

B. Acoustic Characterization

The peak negative pressure of the 6.5-MHz element was recorded with different excitation voltages. Measurements were recorded at the contrast imaging area to verify that this would be the pressure applied in the region of the microbubbles. As shown in Fig. 7, the response of the low-frequency transducer was nearly linear at excitation voltages lower than 70 V, having an average transmitting sensitivity of 14.5 kPa/V. Nonlinearities showed up when the input was higher than 70 V. At about 100 V, more than 1.2 MPa rarefractional pressure (MI: 0.48) was generated, which was sufficient to produce a high-frequency broadband response from microbubbles imaged in tissue in prior studies [16], [17].

Pulse–echo experiments illustrated the broad bandwidth of the receiving element [Fig. 8(b)]. The pulse length of the echo signal was about 80 ns (at −20 dB), corresponding to an axial resolution of 60 µm in tissue, which means that the high-frequency transducer can be used in pulse-echo mode for high-resolution fundamental imaging. The −6 dB fractional bandwidth of the receiving element was measured to be 58.6%, covering a frequency span of 20 to 38 MHz, providing good reception of the high-frequency, broadband microbubble response. Because of the frequency selective isolation layer, the high-frequency element behaves as if there was little backing for it. As such, the bandwidth predicted by the modeling result was broad [Fig. 8(a)] and is seen in the measured bandwidth [Fig. 8(b)]. Burst excitation showed that the loop sensitiv-
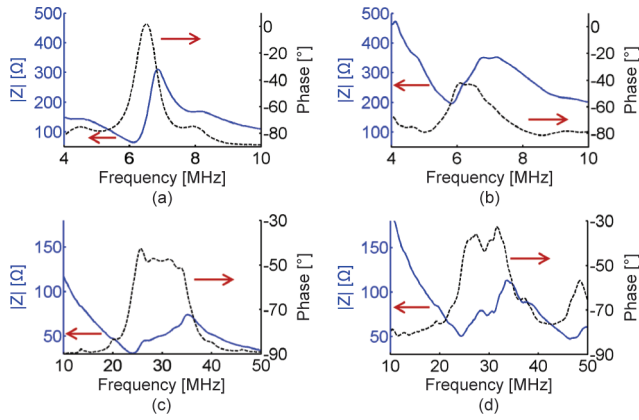
Fig. 6. Electrical impedance of the [(a) and (b)] 6.5-MHz element and [(c) and (d)] 30-MHz element from [(a) and (c)] KLM modeling and [(b) and (d)] measurement from impedance analyzer.

ity of the receiving element relative to the transmitting element was −38.3 dB.

The transmit frequency spectrum was measured by hydrophone using a 2-cycle burst excitation, and the receive bandwidth was measured from the pulse–echo experiment driven with a 1 µJ impulse. The −20 dB frequency response of the transmit element was 4.0 to 8.9 MHz. The frequency response of the transmitting and receiving elements were well separated (>5 MHz at −20 dB) (Fig. 9), which is ideal for detecting microbubble broadband frequency content and achieving high CTRs.

C. Contrast Detection by the Transducer

Microbubble response was clearly detected with the dual-frequency transducer. In the time-domain amplitude analysis, an rms value through the 100 lines of data was taken as the amplitude of the microbubble response. The received data was first high-pass filtered at 10 MHz to thoroughly remove residual tissue/phantom responses at the fundamental or low harmonic frequencies. Residual
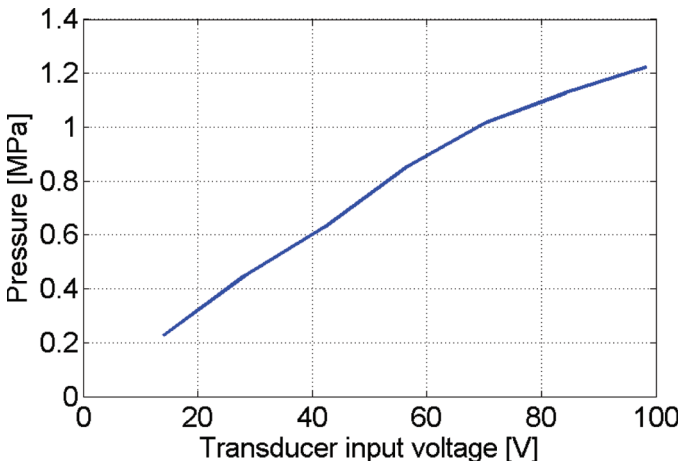

Fig. 7. Peak rarefractional pressure at the contrast imaging area, 3 mm away from the center of the transducer, using a 5-cycle burst excitation on the low-frequency (6.5-MHz) element at varied voltages.
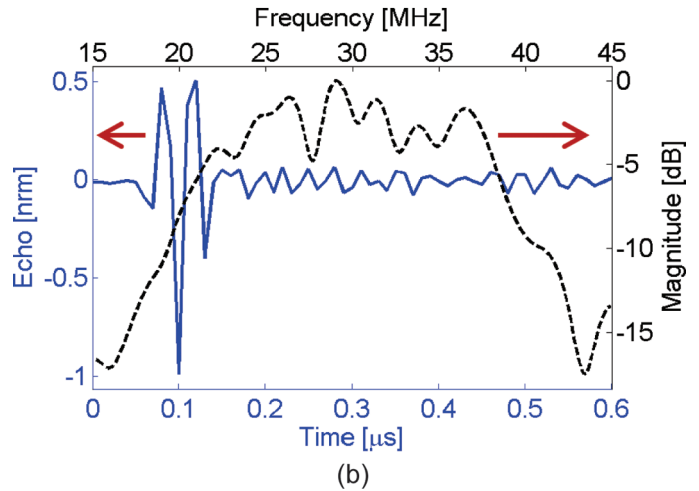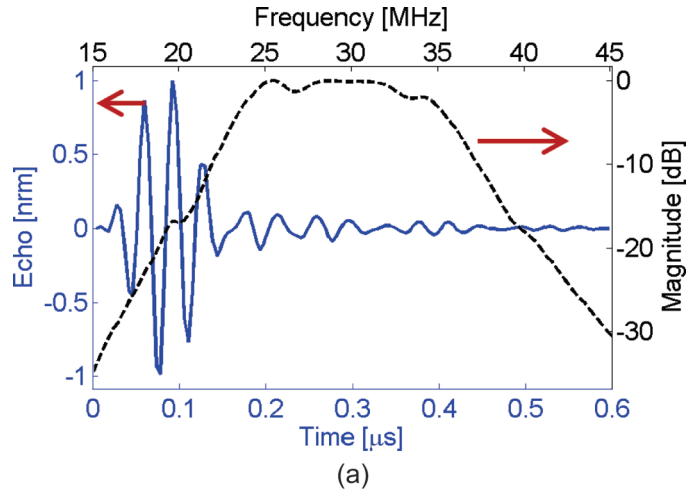

Fig. 8. Pulse-echo response and its fast Fourier transform spectrum of the 30-MHz element in (a) modeling and (b) measurement.

stationary signals from the tube wall were filtered using a clutter filter, leaving only the transient high-frequency signal from microbubbles. RMS values of the microbubble response with different excitations are shown in Fig. 10. As shown in the figure, the background noise was about 0.5 mV, the source of which is primarily the noise of the amplifier. With 1-cycle burst excitation, the peak negative pressure was low (PNP <0.65 MPa) at all voltage inputs (14 to 98 V), resulting in low (6 dB) SNR [Fig. 10(a)]. With 2 or more cycles in each burst, microbubble response could be more than 1.5 mV at 70 V excitation (PNP ≥0.8 MPa), and the SNR was larger than 10 dB [Figs. 10(b) and 10(c)]. Because of the small Q-factor of the receiving element, each negative peak of the transmission wave was clearly discernible temporally [Fig. 10(c)]. At 2 or more cycles in each burst, 42 V input excitation was high enough to excite the nonlinear microbubble response (however, at a low SNR of 4 dB), corresponding to a rarefractional pressure of 0.65 MPa. The microbubble response was just slightly higher at 98 V input compared with 70 V input, and we hypothesize that increasing the pressure to a level that is too high may decrease the CTR because of increased nonlinear response in tissue. No sig-
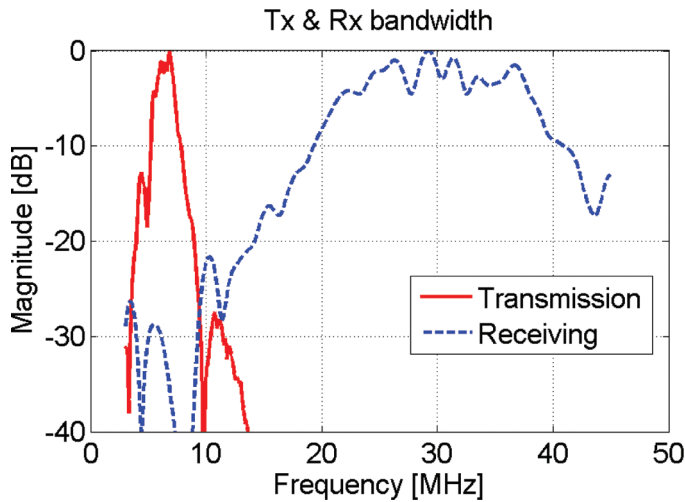
Fig. 9. Transmission (2-cycle burst) and receiving (pulse–echo) bandwidth separation.
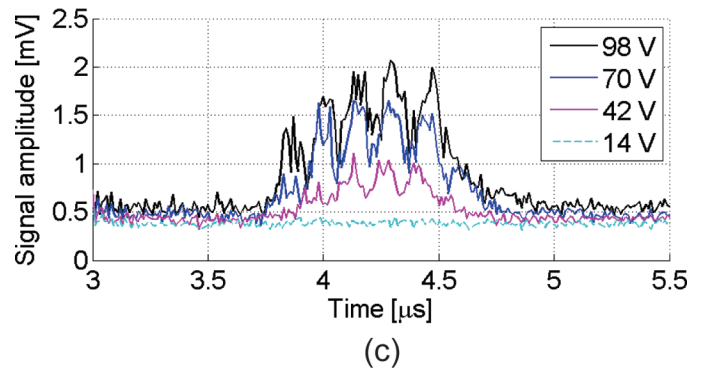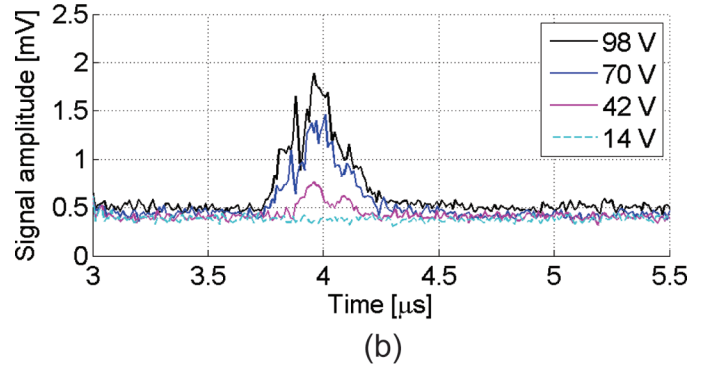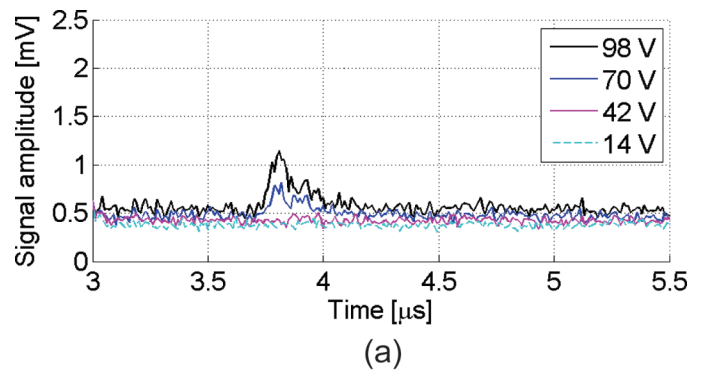

Fig. 10. Amplitude of nonlinear microbubble response with sinusoidal bursts of (a) 1 cycle, (b) 2 cycles, and (c) 5 cycles at different voltage excitations.

nal was detected at low-level voltage excitation (14 V) and the response was always within the noise. In summary, up to an input voltage of 70 V, the SNR increased rapidly with increasing driving voltage and then leveled off. If the input voltage was higher than 70 V, the signal increase of the microbubble response was less significant. Gessner *et al.* also observed a similar plateau for nonlinear microbubble response as a function of pressure when excited at 2 MHz [25]. The excitation voltage may be further optimized for *in vivo* conditions.

The spectra of the received signals were analyzed to investigate the microbubble response in frequency space. Spectra of all 100 measurements were calculated using the short-time Fourier transform and the spectrum for a given test condition was analyzed. As shown in Fig. 11, frequencies lower than 20 MHz were intrinsically suppressed by the transducer's receiving sensitivity, so low-frequency harmonics of the fundamental do not greatly contribute to the image formation in dual-frequency imaging. Input voltage was kept at 70 V while the number of cycles in the burst was varied (Fig. 11). Bursts with fewer cycles produced higher axial resolution; however, a 1-cycle burst suffered from low SNR because the peak negative pressure was too low to induce sufficient microbubble harmonics. With a 2-cycle burst at 70 V input, microbubble response was detected while minimizing loss of axial resolution (about 200 μm). The frequency content of the noise was less than −12 dB relative to the peak frequency content of the microbubble signal [Fig. 11(b)].

The presence of the microbubble signal was verified by rinsing the tube with pure water. The high-frequency response observed when imaging microbubbles vanished instantly when the microbubbles were cleared [Fig. 11(f)].

D. Imaging With the Transducer

1) Fundamental Imaging at 30 MHz: Fundamental imaging mode was performed using the 30-MHz element

in pulse–echo mode. An impulse with 1 μJ energy was used to produce acoustic waves and the reflected signal was recorded by a LabVIEW data acquisition system at 100 MHz sampling rate. The envelope was detected and the magnitude was scan converted to the polar system as shown in Fig. 12. In fundamental imaging mode, the reflection from the 0.6-mm steel rod was nearly 20 dB stronger than that from the 200-μm tube containing microbubbles.

2) Super-Harmonic Imaging: In the dual-frequency imaging mode, microbubbles were excited using the low-frequency element and backscatter was received using the 30-MHz element. The transmission input was a 6.5 MHz 2-cycle sinusoidal burst at 84 V. The received signal was high-pass filtered at 10 MHz before being digitized.

The data was filtered digitally and reconstructed to create an image offline in Matlab. First, each line in the scan was band-pass filtered with a 60th-order finite impulse response filter with corner frequencies of 25 and 35 MHz, which is also the sensitivity range of the transducer. The frequency content in this bandwidth covers the majority of the fourth and fifth harmonics of the transmission frequency. After filtering, the wave package was detected from the signal and the magnitude was scan converted to polar coordinates as shown in Fig. 13.

The microbubble-filled tube was clearly detected and had a CTR of 12 dB. There was some nonlinear response from the rod, signified by its presence in the image even after filtering, but the signal magnitude was strongly decreased in comparison to the fundamental-mode image. In dual-frequency imaging, the microbubble response was almost the same magnitude as the reflection from the steel rod. Because the sound speed in steel is about 4 times of that in water, the reflection from the back surface of the steel rod seems very close to the reflection from the front surface, introducing a high distortion in the axial resolution on the rod.

IV. CONCLUSION

In this paper, a dual-frequency IVUS transducer was designed, fabricated, and characterized, and its contrast imaging and fundamental imaging capability were evaluated. The measured transducer performance matched the modeling results very well for both transmission and receiving components.

In the transducer design, two key features were proposed. First, the aperture of the receiving element was significantly smaller than the transmission element, enabling matched electrical impedance of both elements and matched acoustic impedance on transmit for increased acoustic deposition in the imaging field of view. Second, the isolation layer placed intermediately between the two active layers enabled the low-frequency transmit wave to pass through the isolation interface, but the high-frequency receive wave to be reflected, which aided in decoupling signal content. Thickness of the isolation layer was controlled by mixing a 1% microsphere (10 µm diameter) solution into the silver epoxy. The addition of the microspheres had little effect on the acoustic or electrical
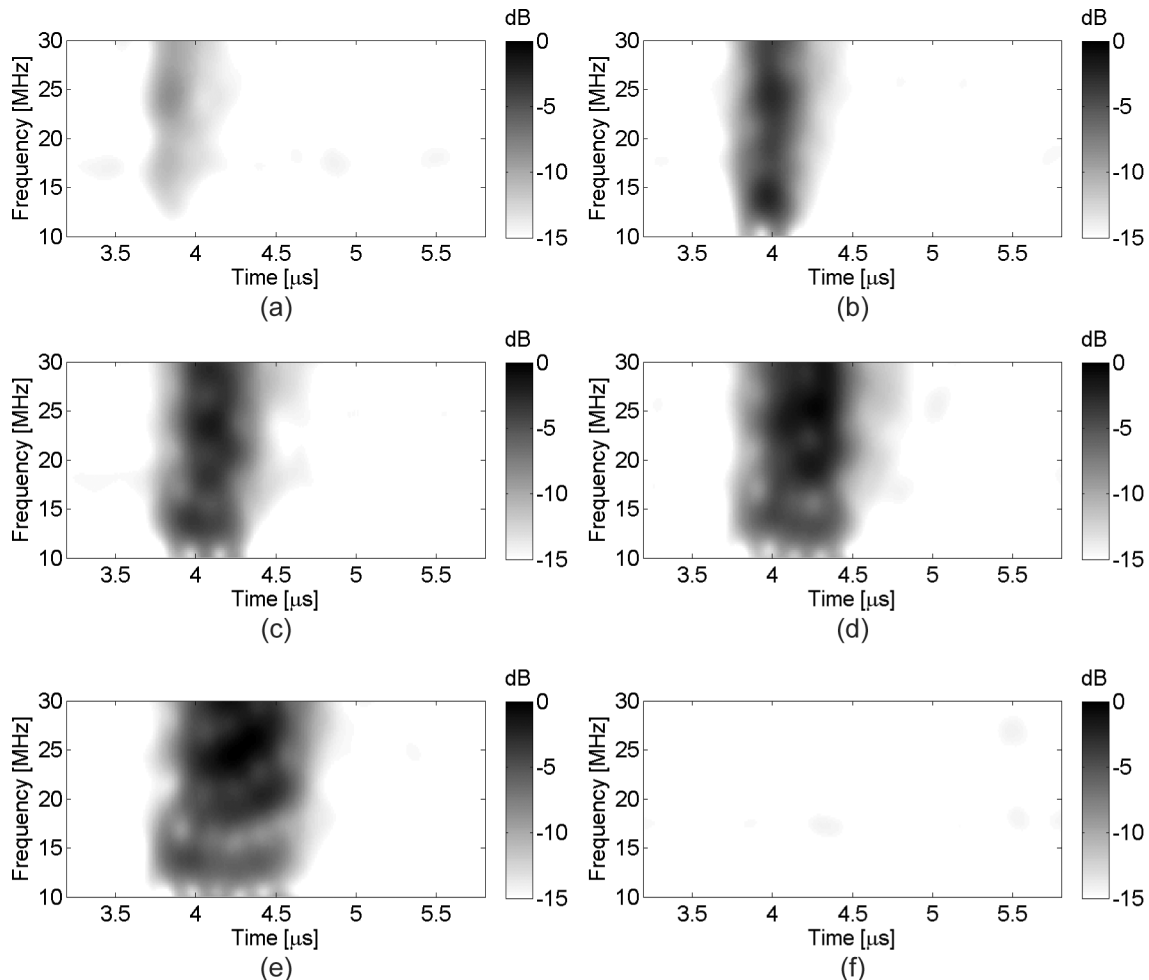

Fig. 11. Spectrum of microbubble responses at 70 V with a burst of (a) 1 cycle, (b) 2 cycles, (c) 3 cycles, (d) 4 cycles, and (e) 5 cycles. The spectrum of a water-filled tube at 70 V with a burst of (f) 5 cycles is shown for comparison.
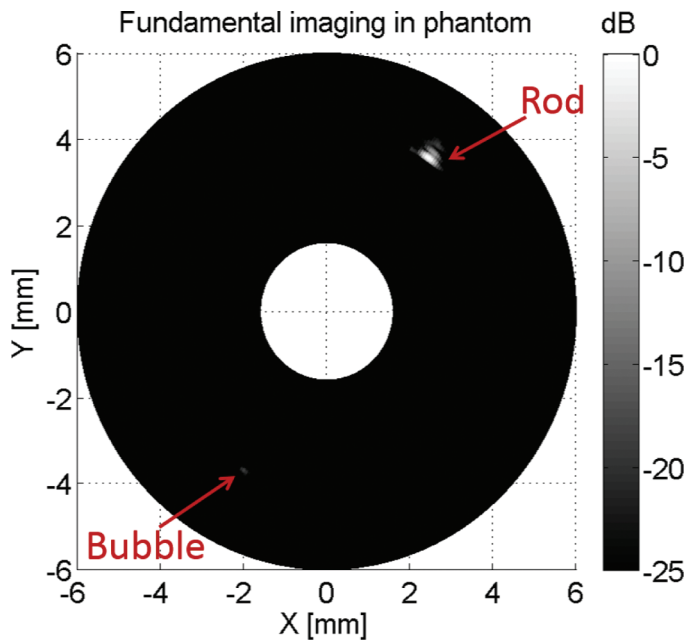
Fig. 12. Fundamental imaging at 30 MHz.

properties of the silver epoxy. Finally, a layer of parylene coating acted both as shielding and as the matching layer of the high-frequency receiver. Such design and fabrication processes were demonstrated to be successful in prototyping dual-frequency transducers for both fundamental-mode imaging and contrast-specific imaging.

The feasibility of ultra-broadband contrast enhanced intravascular ultrasound imaging was evaluated *in vitro*, using a unique prototype dual-frequency small-aperture transducer (T6.5/R30). Peak negative pressures higher than 1.2 MPa were generated at 3 mm away axially from the low-frequency element (0.6×3 mm) of the transducer, which proved sufficient for contrast imaging. Sensitivity of the receiving element (0.6×0.5 mm) provided the capability to detect and record the broadband high-frequency response of microbubbles. Initial imaging of a 200-µm tube filled with microbubbles showed reasonably high SNR (>12 dB). The small-aperture dual-frequency transducer design presented demonstrates the first of its kind for contrast-enhanced high-frequency ultra-broadband intravascular imaging.

Both fundamental mode and dual-frequency super-harmonic imaging were tested *in vitro* using a tissue-mimicking gelatin-based phantom. The 30 MHz pulse–echo fundamental imaging showed a very high SNR (>25 dB) with reasonable resolution (200 µm). Although microbubble backscatter was very weak in the fundamental mode, dual-frequency super-harmonic imaging generated high CTR (12 dB) and good resolution (200 µm) in resolving the microbubble-filled tube. The steel rod used in the experiments was an extremely exaggerated target with a reflection coefficient of 0.94 in water, thus the strength of the echo was large enough that weak high-frequency components of transmission were detectable. Because of

the viscoelastic behavior of tissue, we would not expect to detect tissue harmonics in the high-frequency bandwidth at the transmission acoustic pressure levels (MI <0.48 at 6.5 MHz) used in these experiments. Contrast agent detection in high fidelity is necessary for microbubble imaging strategies used in both molecular imaging and vasa vasorum localization. Small-aperture transducers with high CTR and high resolution capable of detecting contrast agents would promote the transition of advanced contrast-imaging methods to intravascular ultrasound applications.

Although these results are promising, there are still improvements to be made in the near future. The noise level in the measurements was high (0.5 mV), resulting in an SNR lower than 20 dB in super-harmonic imaging. This noise may have come from several different sources, such as the transducer, cabling, or the amplifier. It is anticipated that further isolating the power amplifier used in the transmission circuitry when receiving will likely decrease the noise level and improve the CTR and SNR. Digital signal processing methods, such as wavelet denoising, could also be employed to remove the broadband white noise from the amplifier efficiently. Additionally, it is believed that further improvement can be made by exploring other piezoelectric composites (PMN-PT 1–3) that have been considered previously for intravascular applications [32]. Because of its low acoustic impedance and high electro-mechanical coupling coefficient, PMN-PT 1–3 transducers generally have a broader frequency bandwidth and a higher receive sensitivity. In conclusion, the small-aperture dual-frequency IVUS transducer presented in this paper suggests promising advances in contrast-enhanced IVUS imaging.
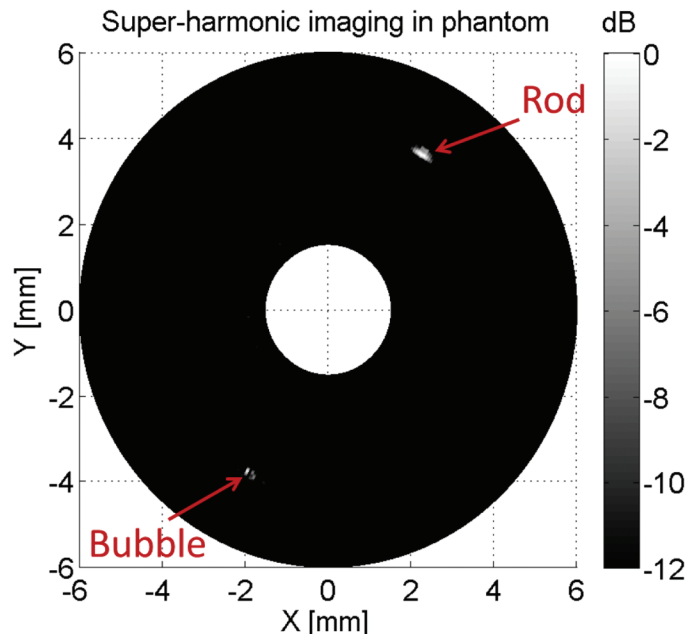

Fig. 13. Super-harmonic imaging of the microbubble tube and a steel rod.

Acknowledgments

The assistance of J. Tsuruta is appreciated for his role in contrast agent formulation. The authors also appreciate the advice of T. Nichols, M.D., and R. Stouffer, M.D., from UNC Cardiology for their consultation on IVUS imaging.

References

[1] M. Naghavi, P. Libby, E. Falk, S. W. Casscells, S. Litovsky, J. Rumberger, J. J. Badimon, C. Stefanadis, P. Moreno, G. Pasterkamp, Z. Fayad, P. H. Stone, S. Waxman, P. Raggi, M. Madjid, A. Zarrabi, A. Burke, C. Yuan, P. J. Fitzgerald, D. S. Siscovick, C. L. de Korte, M. Aikawa, K. E. Juhani Airaksinen, G. Assmann, C. R. Becker, J. H. Chesebro, A. Farb, Z. S. Galis, C. Jackson, I. K. Jang, W. Koenig, R. A. Lodder, K. March, J. Demirovic, M. Navab, S. G. Priori, M. D. Rekhter, R. Bahr, S. M. Grundy, R. Mehran, A. Colombo, E. Boerwinkle, C. Ballantyne, W. Insull Jr, R. S. Schwartz, R. Vogel, P. W. Serruys, G. K. Hansson, D. P. Faxon, S. Kaul, H. Drexler, P. Greenland, J. E. Muller, R. Virmani, P. M. Ridker, D. P. Zipes, P. K. Shah, and J. T. Willerson, "From vulnerable plaque to vulnerable patient: A call for new definitions and risk assessment strategies: Part I," *Circulation*, vol. 108, no. 14, pp. 1664–1672, 2003.

[2] R. Glaser, F Selzer, DP Faxon, WK Laskey, HA Cohen, J Slater, KM Detre, and RL Wilensky, "Clinical progression of incidental, asymptomatic lesions discovered during culprit vessel coronary intervention," *Circulation*, vol. 111, no. 2, pp. 143–149, 2005.

[3] D. E. Goertz, M. E. Frijlink, D. Tempel, V. Bhagwandas, A. Gisolf, R. Krams, N. de Jong, and A. F. van der Steen, "Subharmonic contrast intravascular ultrasound for vasa vasorum imaging," *Ultrasound Med. Biol.*, vol. 33, pp. 1859–1872, Dec. 2007.

[4] P. Constantinides, "Cause of thrombosis in human atherosclerotic arteries," *Am. J. Cardiol.*, vol. 66, no. 16, pp. 37G–40G, 1990.

[5] M. Naghavi, *Asympotomatic Atherosclerosis: Pathophysiology, Detection and Treatment.* New York, NY: Humana Press, 2010.

[6] K. S. Moulton, K. Vakili, D. Zurakowski, M. Soliman, C. Butterfield, E. Sylvin, K. Lo, S. Gillies, K. Javaherian, and J. Folkman, "Inhibition of plaque neovascularization reduces macrophage accumulation and progression of advanced atherosclerosis," *Proc. Natl. Acad. Sci. USA*, vol. 100, no. 8, pp. 4736–4741, 2003.

[7] R. Virmani, F. D. Kolodgie, A. P. Burke, A. V. Finn, H. K. Gold, T. N. Tulenko, S. P. Wrenn, and J. Narula, "Atherosclerotic plaque progression and vulnerability to rupture: Angiogenesis as a source of intraplaque hemorrhage," *Arterioscler. Thromb. Vasc. Biol.*, vol. 25, no. 10, pp. 2054–2061, 2005.

[8] F. D. Kolodgie, H. K. Gold, A. P. Burke, D. R. Fowler, H. S. Kruth, D. K. Weber, A. Farb, L. J. Guerrero, M. Hayase, R. Kutys, J. Narula, A. V. Finn, and R. Virmani, "Intraplaque hemorrhage and progression of coronary atheroma," *N. Engl. J. Med.*, vol. 349, no. 24, pp. 2316–2325, 2003.

[9] J. Milei, J. C. Parodi, G. F. Alonso, A. Barone, D. Grana, and L. Matturri, "Carotid rupture and intraplaque hemorrhage: Immunophenotype and role of cells involved," *Am. Heart J.*, vol. 136, no. 6, pp. 1096–1105, 1998.

[10] P. R. Moreno and V. Fuster, "New aspects in the pathogenesis of diabetic atherothrombosis," *J. Am. Coll. Cardiol.*, vol. 44, no. 12, pp. 2293–2300, 2004.

[11] F. A. Jaffer, P. Libby, and R. Weissleder, "Molecular and cellular imaging of atherosclerosis: Emerging applications," *J. Am. Coll. Cardiol.*, vol. 47, no. 7, pp. 1328–1338, 2006.

[12] J. R. Lindner, "Molecular imaging with contrast ultrasound and targeted microbubbles," *J. Nucl. Cardiol.*, vol. 11, pp. 215–221, Mar.–Apr. 2004.

[13] R. P. Choudhury, V. Fuster, and Z. A. Fayad, "Molecular, cellular and functional imaging of atherothrombosis," *Nat. Rev. Drug Discov.*, vol. 3, pp. 913–925, Nov. 2004.

[14] R. Gessner and P. A. Dayton, "Advances in molecular imaging with ultrasound," *Mol. Imaging*, vol. 9, pp. 117–127, Jun. 2010.

[15] G. L. ten Kate, E. J. G. Sijbrands, R. Valkema, F. J. ten Cate, S. B. Feinstein, A. F. W. Steen, M. J. A. P. Daemen, and A. F. L. Schinkel, "Molecular imaging of inflammation and intraplaque vasa vasorum: A step forward to identification of vulnerable plaques?" *J. Nucl. Cardiol.*, vol. 17, no. 5, pp. 897–912, 2010.

[16] R. C. Gessner, C. B. Frederick, F. S. Foster, and P. A. Dayton, "Acoustic angiography: A new imaging modality for assessing microvasculature architecture," *Int. J. Biomed. Imaging*, vol. 2013, art. no. 936593, 2013.

[17] R. C. Gessner, S. R. Aylward, and P. A. Dayton, "Mapping microvasculature with acoustic angiography yields quantifiable differences between healthy and tumor-bearing tissue volumes in a rodent model," *Radiology*, vol. 264, no. 3, pp. 733–740, 2012.

[18] S. B. Feinstein, "Contrast ultrasound imaging of the carotid artery vasa vasorum and atherosclerotic plaque neovascularization," *J. Am. Coll. Cardiol.*, vol. 48, no. 2, pp. 236–243, 2006.

[19] D. Staub, A. F. L. Schinkel, B. Coll, S. Coli, A. F. W. van der Steen, J. D. Reed, C. Krueger, K. E. Thomenius, D. Adam, E. J. Sijbrands, F. J. ten Cate, and S. B. Feinstein, "Contrast-enhanced ultrasound imaging of the vasa vasorum: From early atherosclerosis to the identification of unstable plaques," *JACC Cardiovasc. Imaging*, vol. 3, no. 7, pp. 761–771, 2010.

[20] J. D. Kasprzak, B. Paelinck, F. J. Ten Cate, W. B. Vletter, N. de Jong, D. Poldermans, A. Elhendy, A. Bouakaz, and J. R. Roelandt, "Comparison of native and contrast-enhanced harmonic echocardiography for visualization of left ventricular endocardial border," *Am. J. Cardiol.*, vol. 83, no. 2, pp. 211–217, 1999.

[21] D. E. Goertz, M. E. Frijlink, D. Tempel, L. C. van Damme, R. Krams, J. A. Schaar, J. Folkert, P. W. Serruys, N. D. Jong, and A. F. van der Steen, "Contrast harmonic intravascular ultrasound: A feasibility study for vasa vasorum imaging," *Invest. Radiol.*, vol. 41, no. 8, pp. 631–638, 2006.

[22] N. de Jong, A. Bouakaz, and F. J. Ten Cate, "Contrast harmonic imaging," *Ultrasonics*, vol. 40, no. 1–8, pp. 567–573, 2002.

[23] A. Bouakaz, B. J. Krenning, W. B. Vletter, F. J. Ten Cate, and N. de Jong, "Contrast superharmonic imaging: A feasibility study," *Ultrasound Med. Biol.*, vol. 29, no. 4, pp. 547–553, 2003.

[24] D. E. Kruse and K. Ferrara, "A new imaging strategy using wideband transient response of ultrasound contrast agents," *IEEE Trans. Ultrason. Ferroelectr. Freq. Control*, vol. 52, no. 8, pp. 1320–1329, 2005.

[25] R. Gessner, M. Lukacs, M. Lee, E. Cherin, F. S. Foster, and P. A. Dayton, "High-resolution, high-contrast ultrasound imaging using a prototype dual-frequency transducer: In vitro and in vivo studies," *IEEE Trans. Ultrason. Ferroelectr. Freq. Control*, vol. 57, no. 8, pp. 1772–1781, 2010.

[26] J. Ma, K. H. Martin, P. A. Dayton, and X. Jiang, "Small aperture, dual frequency ultrasound transducers for intravascular contrast imaging," in *Joint UFFC, EFTF, and PFM Symp.*, 2013, pp. 769–772.

[27] T. Azuma, M. Ogihara, J. Kubota, A. Sasaki, S. I. Umemura, and H. Furuhata, "Dual-frequency ultrasound imaging and therapeutic bilaminar array using frequency selective isolation layer," *IEEE Trans. Ultrason. Ferroelectr. Freq. Control*, vol. 57, no. 5, pp. 1211–1224, 2010.

[28] R. Krimholtz, D. A. Leedom, and G. L. Matthaei, "New equivalent circuits for elementary piezoelectric transducers," *Electron. Lett.*, vol. 6, no. 13, pp. 398–399, 1970.

[29] H. M. Garcia-Garcia, M. A. Costa, and P. W. Serruys, "Imaging of coronary atherosclerosis: intravascular ultrasound," *Eur. Heart J.*, vol. 31, pp. 2456–2469, Oct. 2010.

[30] K. K. Shung, J. M. Cannata, and Q. F. Zhou, "Piezoelectric materials for high frequency medical imaging applications: A review," *J. Electroceram.*, vol. 19, no. 1, pp. 141–147, 2007.

[31] M. A. Borden, M. R. Sarantos, S. M. Stieger, S. I. Simon, K. W. Ferrara, and P. A. Dayton, "Ultrasound radiation force modulates ligand availability on targeted contrast agents," *Mol. Imaging*, vol. 5, pp. 139–147, Jul. 2006.

[32] J. R. Yuan, X. Jiang, P.-J. Cao, A. Sadaka, R. Bautista, K. Snook, and P. Rehrig, "High frequency piezo composites microfabricated ultrasound transducers for intravascular imaging," in *IEEE Ultrasonics Symp.*, 2006, pp. 264–268.
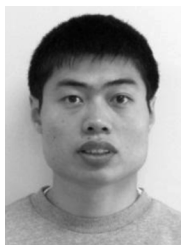
Jianguo Ma received his B.S. and M. S. degrees in 2008 and 2011, respectively, from the School of Physics, Shandong University in China, working on bat biosonar research. In 2011, he joined Dr. Xiaoning Jiang's Micro/Nano Engineering Lab at North Carolina State University, working on the design and fabrication of piezoelectric ultrasound transducers which are used for diagnosis and non-invasive therapy. He is also interested in RF and microwave circuit design involving transmission lines, antennas, filters, and matching networks.

Heath Martin obtained his B.S.E. degree in 2009 from Mercer University, where he performed research in computational fluid dynamics, finite element method, and cardiovascular rheology. Heath joined the Dayton lab in 2011 after working for a private Department of Defense contractor in aerospace. He has a broad research interest in applications to enhance diagnosis and therapy for patients with cardiovascular diseases.

Paul Dayton received his B.S. degree in physics from Villanova University in 2005, his M.E. degree in electrical engineering from the University of Virginia in 1998, and his Ph.D. degree in biomedical engineering in 2001, also from the University of Virginia. He pursued postdoctoral research and was later research faculty at the University of California, Davis. Much of Dr. Dayton's training was under the mentorship of Dr. Katherine Ferrara; his initial studies involved high-speed optical and acoustical analysis of individual contrast agent microbubbles. In 2007, Dr. Dayton moved to the Joint Department of Biomedical Engineering at UNC Chapel Hill and NC State University, Raleigh, where he is now Professor and Associate Department Chair. Dr. Dayton is currently Associate Director for Education for the Biomedical Imaging Research Center, and his research interests involve ultrasound contrast imaging, ultrasound-mediated therapies, and medical devices. Dr. Dayton is a member of the technical program committee for IEEE UFFC, and a member of the editorial boards for the journals *IEEE Transactions on Ultrasonics, Ferroelectrics, and Frequency Control*, as well as *Molecular Imaging* and *Bubble Science, Engineering, and Technology*.

Xiaoning Jiang received his B.S. degree in mechanical engineering from Shanghai Jiaotong University in 1990, his M.S. degree in mechanical engineering from Tianjin University in 1992, and his Ph.D. degree in precision instruments from Tsinghua University in 1997. He received postdoctoral training from Nanyang Technological University and The Pennsylvania State University from 1997 to 2001. He joined Standard MEMS Inc. as an R&D Engineer in 2001 and then worked for TRS Technologies Inc. as a Research Scientist, Senior Scientist, Chief Scientist, and Vice President for Technology before joining North Carolina State University in 2009 as an Associate Professor of Mechanical and Aerospace Engineering and an Adjunct Professor of Biomedical Engineering. Dr. Jiang is the author and co-author of two book chapters, one book, six issued US patents and more than 10 US patent applications, more than 40 peer-reviewed journal papers, and more than 60 conference papers on piezoelectric composite micromachined ultrasound transducers, ultrasound for medical imaging and therapy, NDE, smart materials and structures, and M/NEMS. Dr. Jiang is a member of the technical program committee for IEEE UFFC. He is also a Guest Editor for the journal *Sensors*.